

Customizable Fabrication for Auxetic Graphene Assembled Macrofilms with High Conductivity and Flexibility

Peng Li^{a,1}, Zhe Wang^{a,1}, Rongguo Song^a, Wei Qian^a, Pin Wen^{b,}, Zhugen Yang^c and Daping He^{a,d,*}*

^a Hubei Engineering Research Center of RF-Microwave Technology and Application, School of Science, Wuhan University of Technology, Wuhan 430070, China

^b Hubei Key Laboratory of Theory and Application of Advanced Materials Mechanics, School of Science, Wuhan University of Technology, Wuhan 430070, China

^c Cranfield Water Science Institute, Cranfield University, Cranfield, MK43 0AL, United Kingdom

^d State Key Laboratory of Advanced Technology for Materials Synthesis and Processing, Wuhan University of Technology, Wuhan 430070, China

¹ These authors contributed equally to this work.

* Corresponding author. E-mail:

Tel: +86 17764003619

* Corresponding author. E-mail: hedaping@whut.edu.cn (Daping He)

Tel: +86 17764000852

Abstract

Auxetic materials with negative Poisson's ratios unusually exhibit intuitive mechanical behaviors, such as cross-section expansion instead of contraction during tension. Such behaviors are interesting because they may enhance unusual mechanical properties. However, controllable preparation of materials with negative Poisson's ratio is still a major challenge. In this study, we report the synthesis of a flexible auxetic graphene assembled macrofilm (GAMF) from graphene oxide nanosheets by a thermal annealing and press assistant method. The obtained materials exhibit good flexibility and significantly wide tunable negative Poisson's ratios ranging from -0.11 to -0.53. We also develop a reconstruction model for characterization the uniaxial tension of GAMF based on X-ray tomographic images. The tensile simulation result predicts the function relationship between Poisson's ratio and critical thickness of pore channels, which is in good agreement with the experimental data. As a result, an effective tunable way is proposed for customizable fabrication of GAMF with tunable negative Poisson's ratios, and the GAMF materials with good flexibility, high electrical conductivity and superior auxetic behavior looks promising for future development of wearable electronics.

Keywords: Auxetic materials, negative Poisson's ratio, porous graphene film, prediction of tunable Poisson's ratio

1. Introduction

The Poisson's ratio is a fundamental property of materials describing the negative ratio of transverse strain to applied axial strain [1]. Compared to most conventional materials with positive Poisson's ratio, auxetic materials with negative values Poisson's ratio would expand instead of shrinking at cross section when stretched under uniaxial tension. Materials with such counterintuitive behavior has drawn increasing attention due to the enhanced mechanical properties, such as shear resistance, fracture toughness and energy absorption. These features lead to broad applications in tissue scaffold [2], intelligent sensors [3], protective equipment [4], and national defense engineering [5]. Since reentrant metal foam structure with negative Poisson's ratio has been reported by Lake et al. in 1987 [6], geometric considerations have been extensively studied to design new auxetic materials [7-10]. Artificially designed auxetic effects have so far been seen in numerous crystalline foams [11, 12], microporous polymers [1, 13], metal networks [6, 14, 15], and origami structures [9, 16, 17].

Graphene, consisting of a layer of carbon atoms arranged in a honeycomb lattice, is regarded as one of the most prospective materials of 21st century. However, the one-atom-thick graphene sheet is still difficult to be applied in practice due to the limitations of preparation accuracy and processing difficulty. In recent years, graphene assembled macrofilms (GAMF) prepared from graphene oxide (GO) as raw material has attracted increasing attention. Because of its excellent mechanical properties, lightweight, super high thermal conductivity and electronic conductivity, the GAMF has been studied in the fields of membrane separation, flexible storage and wearable RF devices. However, most previous reports focused on mechanical strength and flexibility, electrical conductivity and thermal conductivity but a little attention has been paid to the Poisson's ratio of GAMF. Molecular dynamic simulation by Grima et al. revealed that vacancy defect in C-C bonds may lead to

graphene wrinkling to the extent to exhibit auxetic behavior [18,19]. Other simulation works manifested rippled graphene [20, 21], porous graphene structure [22], graphene-based carbon foam [23], graphene-based diamond-like phases [24, 25] and disordered graphene layers [26] that may lead to nano architecture auxetic materials. These works stimulated further ongoing research, especially studies based on experimental synthesis [27]. More recently, Wen et al. obtained graphene films with tunable negative Poisson's ratio (NPR) ranging from -0.25 to -0.55 [28]. However, it still remains challenging to find out the mechanism in the hierarchically nano- and microstructures.

In this work, porous auxetic GAMF was successfully prepared by a thermal annealing and press assistant method. The as-obtained materials exhibited a wide tunable negative Poisson's ratios customized from -0.11 to -0.53. The mechanisms behind the auxetic behaviors were clarified by simulation of real specimens, and the possible influencing factors on NPR performances were tested using GAMFs with different critical thicknesses. Moreover, extra-high conductivity of GAMF endowed by annealing would be beneficial to the design and fabrication of different auxetic microstructures for various applications such as intelligent wearable electronic sensors.

2. Experimental

2.1 Preparation of GAMF

Suspensions of GO with solid contents of 2%-4% were first stirred rapidly (400 rpm) for 4 h. The formed GO gel was then poured into a glass mold and left to dry at room temperature. The evaporation of water helped forming GO film with a thickness ranging from 50-80 μm and an average lateral size of 33.6 μm (Fig. S8), which was then peeled off and annealed at 1300 $^{\circ}\text{C}$ for 2 h and 3000 $^{\circ}\text{C}$ for 1 h under argon shielding gas with a heating rate of +10 $^{\circ}\text{C}/\text{min}$. After cooling down to room temperature, GAMF was obtained. To get

various GAMF specimens with different porosities, pressure was applied with 0 MPa, 1 MPa, 5 MPa, 10 MPa, 20 MPa and 50 MPa respectively.

2.2 Measurement of conductivity

Square resistances of GAMF specimens were measured by RTS-9 with 4 point probes. And the conductivities were calculated by $s=1/DR$ (s is the conductivity, D is the thickness and R is the square resistance of GAMF).

2.3 Poisson's ratio Testing

All copper, PET film and GAMF specimens were cut into dumbbell-shape for tension testing by laser engraver (LPKF ProtoLaser R). The gauge length was 50 mm and width was 10 mm. The tension tests were conducted by a universal testing machine (Instron 5848) at speed of 0.4 mm/min. A Non-Contact Full-Field 3D Strain Measurement System (Correlated Solution Inc., VIC-3D) was used to record the 3D deformation of speckled specimens. More mechanics properties (failure stress, modulus, ultimate strain, rigidity and toughness) could also be obtained by the test above (Fig. S9).

2.4 Microstructure characterization

Considering that cutting might break the instinct interface of the film, all specimens were immersed in liquid nitrogen to stabilize the microstructure before cutting. Based on the optical microscope images taken by Olympus IX73, lateral size of resultant GO sheets was calculated by professional software (Image J). SEM images were captured to demonstrate the cross-sections of GO film and GAMF. 3D surface morphology of GAMF was reconstructed by digital microscopy (KEYENCE, VHX-600E), and microstructure of GAMF was reconstructed by professional software (ImageJ and Avizo) using Micro-CT images recorded by 3D X-ray microscope (Carl Zeiss, Xradia 510Versa).

3. Results

As shown in Fig. S1, GAMF was fabricated by annealing graphene oxide (GO) film transformed from GO suspension [29]. At the start of annealing, the absorbed water first evaporated. As temperature further rose, the interlayer and crystal water became fully evaporated. At 3000 °C, some carbon atoms collapsed with oxygen-containing functional groups and converted into gaseous carbon oxides. During this process, the symmetry of the graphene six carbon atom rings might have been broken, those defects in nano-scales yield to the crumpled sheets and account for the folds on graphene layers in micro-scale [18]. Micro-gasbags then sprouted in graphene sheets during evolution of mentioned gaseous carbon oxides [30]. After cooling to room temperature, graphene sheets kept their deformations and micro-pores, formatting accordingly. The SEM images of cross-sections of GO and rGO films are exhibited in Fig. 1b and Fig. 1c. These features well confirmed the supposition. Fig. 1b showed the GO film with dense and regular morphology. During the annealing treatment it expanded in thickness to yield visible micro-pores in Fig. 1c and turned into GAMF. Fig. 1d and Fig. S10 showed the outstanding flexibility of GAMF with two folded examples. The X-ray diffraction (XRD) patterns confirmed the complete graphitization of GO film with interlayer distance of GAMF around 3.35 Å (Fig. 1e). This could be verified by Raman spectroscopy, depicting 2D, 2G and 2D bands located at 1525 cm⁻¹, 2690 cm⁻¹ and 1297 cm⁻¹, respectively. The ratio of I_D/I_G was estimated to 0.087, indicating GAMF with wonderful crystal structure. Fig. 1f compared the conductivities among GAMF and some macrochemically graphene films. From the histogram we could be informed that conductivity of the GAMFs could be customized with Poisson's' ratio ($2.4 \pm 0.11 \times 10^5$ S/m, $2.19 \pm 0.11 \times 10^5$ S/m, $3.09 \pm 0.15 \times 10^5$ S/m with Poisson's ratio of -0.53, -0.21, -0.11), much higher than chemically graphene films (1.63×10^4 S/m [31], 5.37×10^4 S/m [32] and 1.12×10^5 S/m [33]). It also preserved electromagnetic shielding effectiveness of at least 90 dB [34-36]. This meant that GAMFs could be used in electromagnetic shielding related fields (Fig. S2).

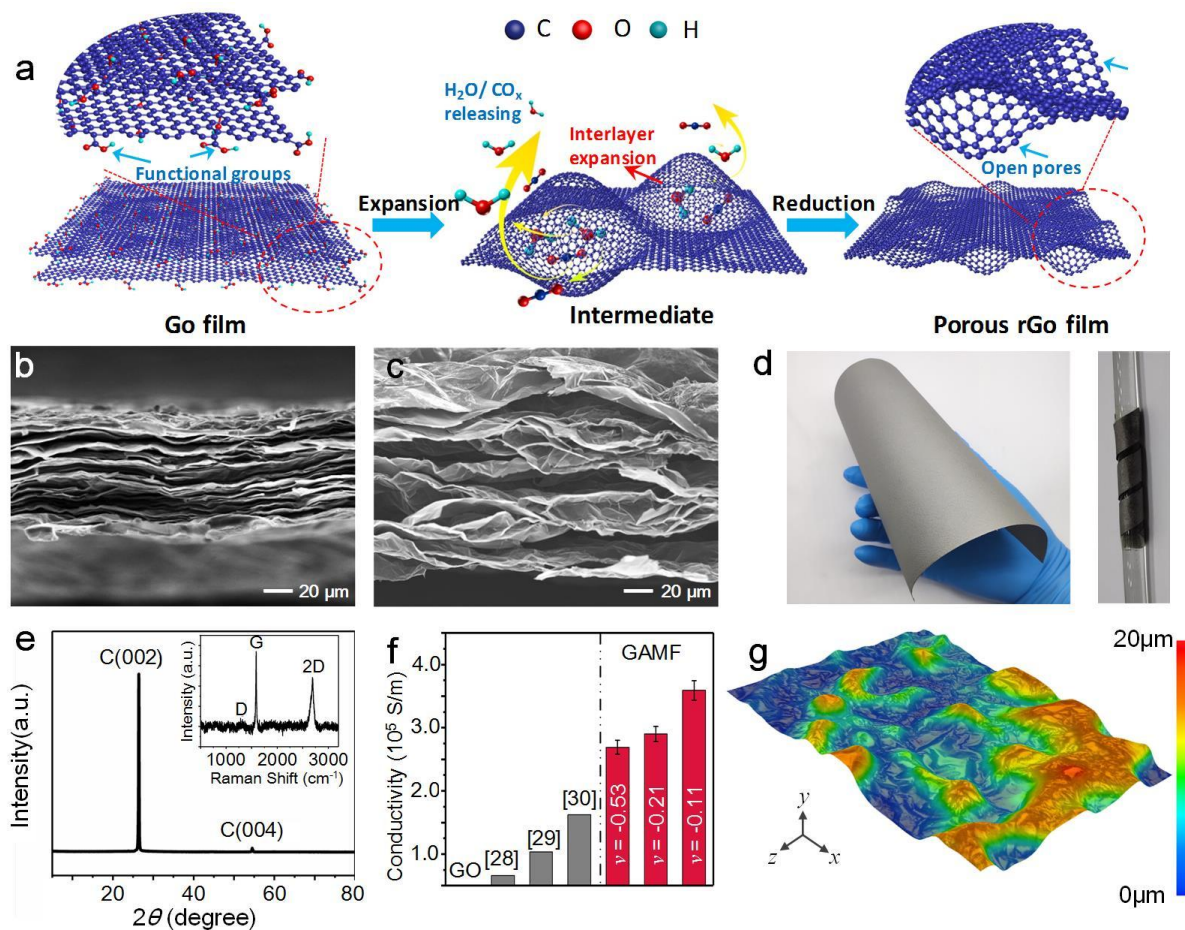


Fig. 1. Structure and characterization of GO and rGO films. a) Schematic illustration of transformation from GO film into porous rGO. b-c) SEM image of cross-section of GO before annealing and rGO film after annealing. d) Folded GAMF examples. e) X-ray diffraction patterns and Raman spectra for rGO film. f) Comparison among conductivities of GAMFs and chemically modified graphene films. g) Three-dimensional reconstruction of surface morphology of rGO film obtained by digital microscopy.

To figure out deformations caused by the Poisson's effect, uniaxial tensions were tested. The structural stiffness would be relatively low for GAMF specimens with thickness around 200 μm , leading to challenging of strain measurements. To obtain accurate Poisson's ratios of GAMF, the universal testing machine and Non-Contact Full-Field 3D Strain Measurement System were used (Fig. 2a). Each GAMF specimen was cut into dumbbell-shape from

fabricated GAMF film and pretreated with speckling by spray. The speckle layer was intentionally kept not thicker than 10 μm to prevent probable effects on stiffness of specimens. Moreover, to prove the reliability of the measurements, copper foil and polyethylene terephthalate (PET) film specimens with known Poisson's ratios (ν_{copper} is about 0.35 and ν_{PET} is around 0.3-0.4, depending on preparation method) were introduced as control group. Conceivably, each specimen in control group was pretreated by speckle as GAMF specimens.

Fig. 2(c and d) exhibits the strain contours of all specimens in transverse and longitudinal directions. Despite strain contours showed concentrated stress in some local areas, negative transverse and positive longitudinal total strain were observed on copper and PET specimens. By contrast, GAMF specimen depicted tension-expansion behavior. The strain fields were positive in both directions, meaning the specimen expanded transversely and longitudinally in uniaxial tension. The Poisson's ratio could be defined as $\nu_{ji} = -\varepsilon_{ii} / \varepsilon_{jj}$. Considering GAMF is anisotropic in y - z and y - x planes but isotropic in x - z plane which means ν_{xz} is equal to ν_{zx} as the x - z coordinates showed in Fig. 2a, we'd like to clarify here that all measured Poisson's ratios in this work indicated ν_{xz} or ν_{zx} . Consequently, auxetic performance indicated GAMF with negative Poisson's ratio graphene structure. For further analysis, six virtual extensometers were introduced to obtain the average strain of specimens. Three specimens (E0, E1, E2) were set in longitudinal direction and others (E3, E4, E5) in transverse direction (Fig. 2b).

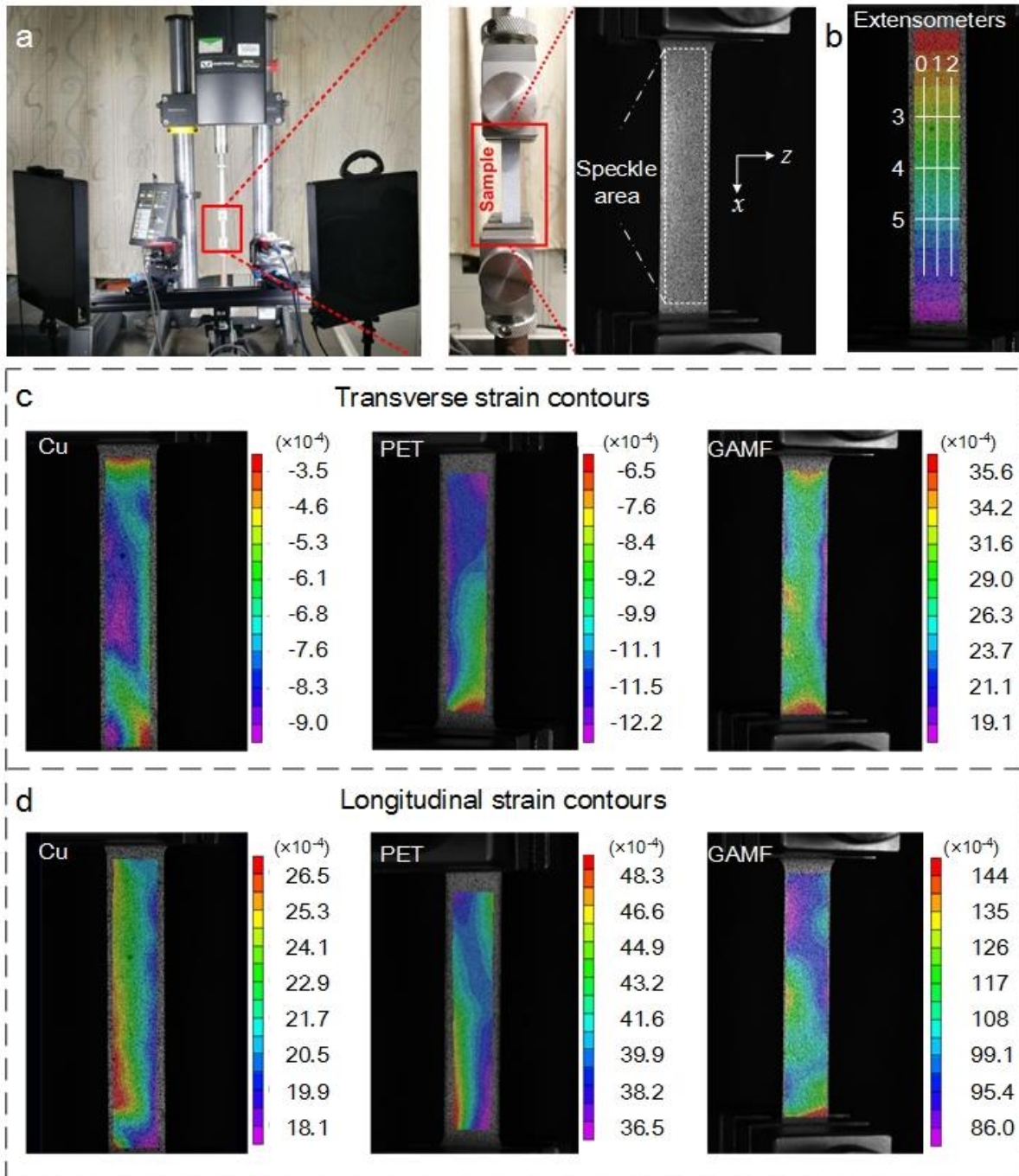


Fig. 2. Uniaxial tension testing for copper, PET, and GAFM specimens. a) Photos of specimen with speckles loading on testing machine. b) Virtual extensometers in deformation measurement system. c,d) Transverse and longitudinal strain contours of copper, PET, and GAFM specimens.

The data shown in Fig. 3 were obtained when considering the deformation data from virtual extensometers. As shown in Fig. 3a, couple HD cameras were set in front of the specimen with speckles [37, 38]. After calibration, contrastive analyses were continuously executed by the system to capture changes in relative position among speckles caused by deformation of the specimen. Based on images snapshotted by both synchronous cameras and DIC algorithm, three-dimensional deformation data were recorded. It is necessary to note that the strain values shown in Fig. 3 are all reported in percentage form. Fig. 3(c and d) exhibits the test results of copper foil and PET film specimens. The stress-strain curves of copper showed that longitudinal strain increased from 0 to about 0.4% as tensile load in elastic stage enhanced. The transverse strain decreased from 0 to about -0.14% due to Poisson's effect. The averaged values of longitudinal and transverse strain allowed to draw $\varepsilon_l-\varepsilon_t$ curve. The Poisson's ratio of copper foil specimen was estimated from the slope of $\varepsilon_l-\varepsilon_t$ curve in dotted area to 0.34 (Figure 3f), consistent with practical values. Analogously, the Poisson's ratio of PET film specimen was recorded as 0.24 (Fig. 3g). The Poisson's ratio matched well with practical value given the effect on mechanical properties of PET caused by different manufacturing processes. Hence, the measurement of Poisson's ratio was pretty reliable. Fig. 3e provides the mechanical behaviors of GAMF specimens. As discussed previously, GAMF displayed auxetic performance, in which the mechanical behavior in transverse direction was similar to that in longitudinal direction but with lower slope. From $\varepsilon_l-\varepsilon_t$ curve, the Poisson's ratio of GAMF in plane was estimated to -0.27.

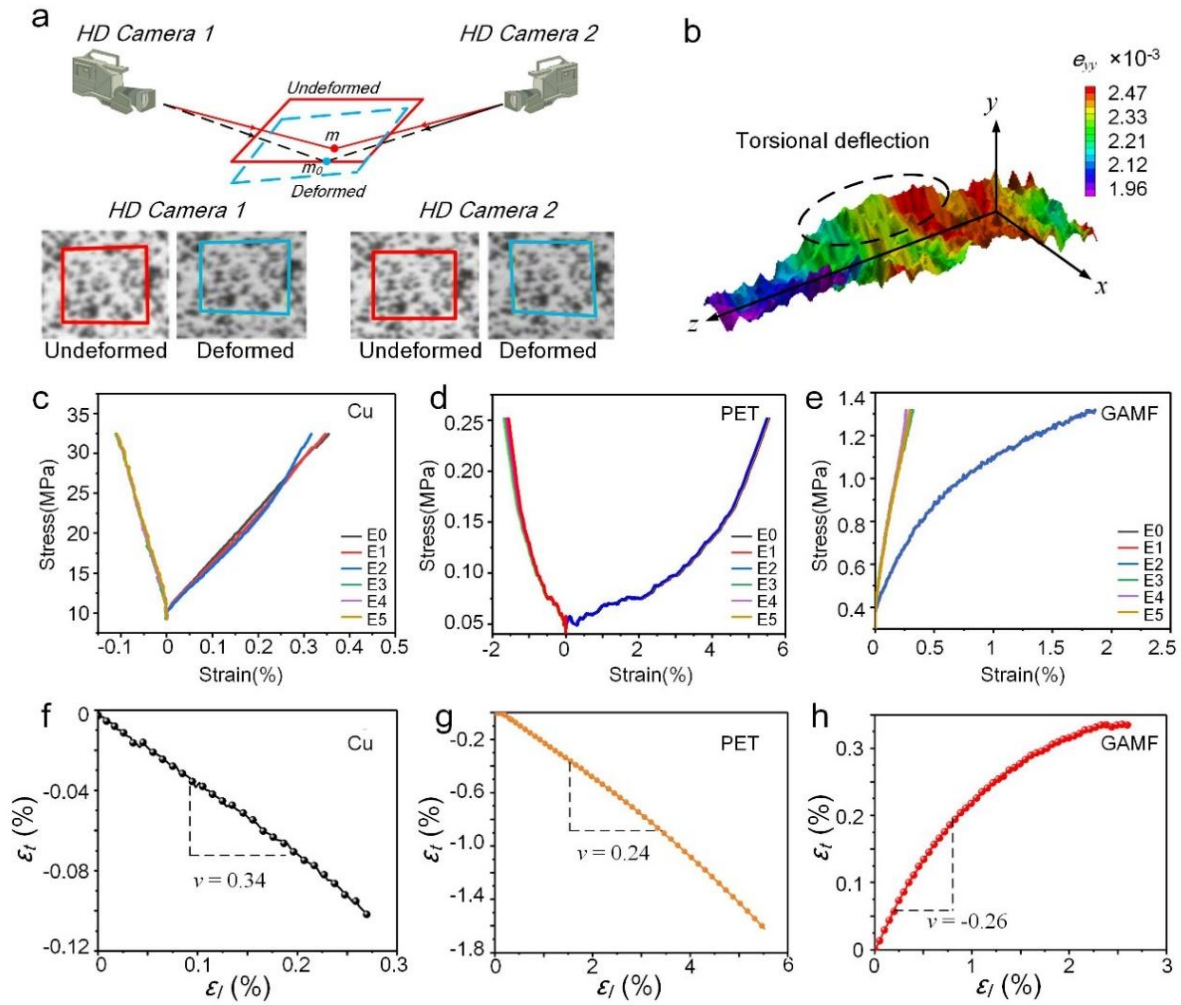


Fig. 3. Test results of Poisson's ratio for all specimens. a) Schematic representation of strain measuring system. b) 3D analysis of specimen deformation during testing. c,d,e) Stress-strain curves of copper, PET, and GAMF specimens. f,g,h) ϵ_t - ϵ_l curves of copper, PET, and GAMF specimens.

The origin of negative Poisson's ratio could be explained through the mechanistic summary at microscale. Fig. 4 illustrates the relationship between the microscopic structure and negative Poisson's ratio, where displacement increment in longitudinal direction was accompanied by displacement expansion in transverse direction. For clarity, the transverse direction was defined as X-direction, elevational direction as Y-direction, and longitudinal direction as Z-direction. Based on X-ray morphology scans we were able to establish a

reliable model instead of assumed model [39]. Over 1000 pieces of tomography images were obtained to clarify the interior morphology of pores (Fig. S3) and a good inter-connectivity was noticed. For analysis and visualization purposes of pore channels, referential values of local thickness were computed and generated color-coded meshes by ORS Visual software. The thickness was calculated as diameter of a hypothetical sphere fitting each boundary point with distribution shown in Fig. 4(a-b). The porosity for one specimen was quantified at 71.54%. Based on above morphology images (Fig. 4c), facets model was reconstructed as in Fig. 4d, matching with local SEM images (Fig. 1c).

The size of facets model was too big to compute the properties by simulating every detail of the microstructure. Thus, representative volume element (RVE) was extracted along the z -direction from facets model to construct voxel model for analysis (Fig. 4e), in which porosity was calibrated with the value measured from X-ray tomography to neglect the variance from grayscale threshold. The aspect ratio was kept the same as the experimental value. The size of RVE over real specimen showed a scaling ratio smaller than 1/1000. Asymptotic homogenization theory (Supporting Note 1) [40-44] could be employed to compute three-dimensional voxel model with 2.5 million elements and 4.08 million nodes. The 4% tension strain was then applied on right side along z -direction while constraint was put on the other side. This approach eliminated the weak boundary effect when compared to experiment setting. The contour plot in Fig. 4f illustrated the total displacement data in nodal solution. The displacement field along the x and z directions were both positive when symbol U was taken as displacement of node in certain direction, symbol “ l ” as length, “ ε ” as strain, and “ ν ” as Poisson’s ratio. Therefore, negative Poisson’s ratio can be calculated according to Eq. (1) [45]:

$$\nu_{zx} = -\varepsilon_x / \varepsilon_z = -(U_x / U_z) \cdot (l_z / l_x) \quad (1)$$

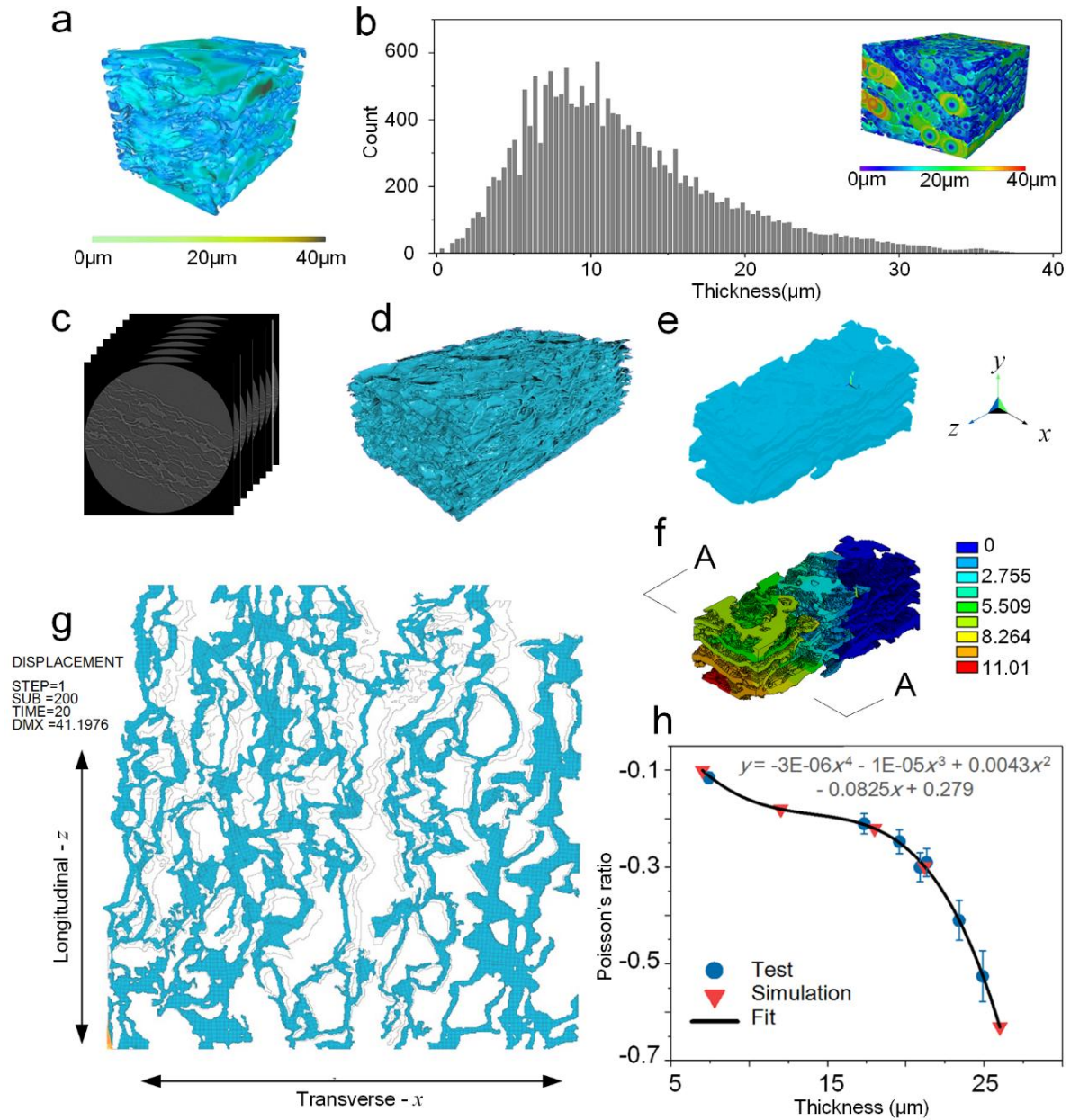


Fig. 4. Simulation-based X-ray morphology images and prediction of relation between Poisson's ratio and microscopic structure. a) Contour plot of thickness distribution of interconnected pores. b) Thickness distribution histogram. c) Micro-CT images by X-ray microscopy. d) Re-constructed facets model. e) Representative volume element in voxel model. f) Contour plot for nodal solution. g) Deformed and undeformed plots for cross-section A from voxel model. h) Prediction of relationship between Poisson's ratio and porosity.

For more clarifications, deformation results of A-A cross-section on xz plane were analyzed (Fig. 4g), where the original outline of RVE was depicted by the hollow area and outline of deformed RVE by solid area. Fig. 4g vividly depicts the auxetic behavior of GAMF under applied load. Note that elongation in z -direction was accompanied by expansion in x -direction. In addition, re-entrant holes were visible throughout the in-plane slices of X-ray Tomography (Fig. S4). However, more insights should be given to re-entrant in-plane holes in slices of microstructure, which would lead to negative Poisson's ratio according to previous literature [47].

The qualitative illustration of pores towards uniaxial tension in z -direction showed that neither porosity nor distribution of pores was directly related to Poisson's ratio. In fact, pore thickness and shape play crucial roles in auxetic performance [48]. Therefore, critical thickness c was defined based on thickness distribution of pore channels.

$$F_{t \geq c}^{(micro)} \geq 10\% \quad (2)$$

where $F^{(micro)}$ is the statistical percentage of thickness distribution, and minimum maker c of thickness t is dragged for integration ratio accounting for 10%.

Briefly, larger values of $F^{(micro)}$ should induce more and larger micro-pores. The c value should be determined by at least one experimental result. In this paper, the above experiment with porosity of 71.54% was used to determine $c=21.2 \mu\text{m}$. Next, morphological manipulation for four different models was implemented to dilate and erode the thickness of micro-pores. Critical thicknesses of respectively $c=7, 12, 18, 26 \mu\text{m}$ were obtained (Fig. S5) and similar analyses were performed for the other four models. A nonlinear relationship was observed in Fig. 4h, and relationship between the Poisson's ratio and critical thickness was fitted to polynomial function ($y= a_1x^4+a_2x^3+a_3x^2+a_4x+a_5$). The fitted curve clearly illustrated that the Poisson's ratio decreased from -0.1 to -0.7 as critical thickness rose from 5 to 26 μm .

In detail, the Poisson's ratio decreased slowly for critical thickness ranging from 7 to 18 μm followed by quick slow down from 18 to 26 μm . In sum, the relationship between Poisson's ratio and critical thickness provided a valuable guideline for technical processing and customization of graphene films with desirable NPRs.

Since the customized direction could clearly lead to different NPR behaviors through tunable thickness of pore channels, several other GAMFs with different thickness of pore channels ($c=7.41, 17.33, 19.58, 21.32, 23.4, \text{ and } 24.9 \mu\text{m}$) were fabricated by pressing under 1-50 MPa load. All GAMFs were cut into dumbbell-shape with the same size as the specimens in Fig. 2a. The results of Poisson's ratio of specimens prepared by VIC-3D measurement system in uniaxial tension testing are exhibited in Fig. 4h and Fig. S6, and the SEM images are shown in Fig. S7. Clearly, the Poisson's ratios decreased monotonically with the increment of critical thickness as -0.11, -0.21, -0.25, -0.29, -0.41 and -0.53 respectively. All test data aligned well with the fitting curve of simulation results, implying enhanced NPR performance through incrementing critical thickness.

4. Conclusion

The reduction of graphene oxide by thermal annealing was shown to form porous structure. Wen [28] et al. reported microstructural hierarchy of pristine chemically modified graphene films with featured wrinkles, delaminated close-packed laminates, ordered and disordered stacks that led to remarkable negative Poisson's ratios. Considering the modulating wavy textures of inter-connected network, pre-stretched was applied to endow chemically modified graphene films with controlled negative Poisson's ratio. Huang [46] et al. compared rGO films reduced by HI acid with thermally annealed rGO films and realized obvious differences in microscale structure, which looked tightly packed in rGO films

reduced by HI but porous in thermally annealed films. Hence, the proposed fabrication method of GAMF showed great potential in customizing the Poisson's ratio.

In Fig. 2 and Fig. 3b, thin sheets with hierarchical or fractal wrinkles were observed under two cameras three-dimensional image correlation measurements. Inevitably, preventing slight torsion in thin films was challenging when the specimens were subject to tensile load [48]. During tension process, in-plane displacement caused by torsion might affect the results but three sensors were set to obtain an average values of longitudinal and transverse strains. Moreover, variance from simulation indicated that the influence can be neglected.

In simulations, the reconstruction manipulation of X-ray microscopy images looked typical for processing of such porous materials [49]. Moreover, the scale of RVE over real material was less than 0.001. Hence, asymptotic homogenization algorithm was suitable to simulate RVE of real materials [10, 18]. Although this theory was available for RVE simulation with constraints under periodic boundary conditions, the averaged theoretical formula was utilized in this study. In addition, the selection of RVE position was calibrated to converge for above real materials, and relationship between critical thickness and Poisson's ratio of GAMF was discussed theoretically based on simulations. Most importantly, by adjusting the critical thickness of GAMF with compressibility, the simulation result was validated, claiming out the simulation could be applied in prediction of GAMF and other materials with similar microporous structure.

In conclusion, microporous structure was constructed as determining factor in auxetic performance of fabricated GAMF with high conductivity and outstanding flexibility through graphitization of treated graphene oxide precursor. The uniaxial tension tests with VIC-3D system confirmed the negative value of Poisson's ratio of GAMF. To clarify the mechanical behaviors of auxetic graphene films, reliable simulation model for microstructure was built by reconstruction of images obtained by X-ray microscopy of real specimens. The simulation

results showed that critical thickness had an impact on NPR performance. GAMFs with different critical thicknesses were fabricated and Poisson's ratios ranging from -0.11 to -0.53 were recorded, which aligned well with the predictions and suggesting promising applications in flexible sensor devices and wearable electronic engineering.

Acknowledgements

This work was financed by 2018 National Key R&D Program of China 257, the National Natural Science Foundation of China (Grant No.: 51372186, 51672204, 51701146, 11902232), the Fundamental Research Funds for the Central Universities (WUT: 2017III055, 2018III039GX, 2018IVA095, 2018IB013,193114005) and the National High-tech R&D Program of China (NO. 2013AA031306).

Author contributions

P.L. and Z.W. contributed equally to this work. P.W. and D.H. conceived and directed the project. R.S. and W.Q performed the fabrication and characterizations. Z.Y. revised the manuscript and suggested for details in tests. All authors participated in the discussion of the results, commented on the implications, and fully approved the content of the manuscript.

Appendix A. Supplementary data

The supplementary data related to this article is attached to another file.

References

- [1] Jiang, J. & Park, H.S. Negative poisson's ratio in single-layer black phosphorus. *Nat. Commun.* 5 (2014) 4727.
- [2] Park, Y.J. & Kim, J.K. The Effect of Negative Poisson's Ratio Polyurethane Scaffolds for Articular Cartilage Tissue Engineering Applications. *Adv. Mater. Sci. Eng.* 2013, 1-5 (2013).

- [3] Guo, F., Jiang, Y., Xu, Z., Xiao, Y., Fang, B., & Liu, Y., et al. Highly stretchable carbon aerogels. *Nat. Commun.* 9, 881-889 (2018).
- [4] Choi, J.B. & Lakes, R.S. Design of a fastener based on negative Poisson's ratio foam. *Cell. Polym.* 10, 205-212 (1991).
- [5] Alderson, A. A triumph of lateral thought. *Chem. Ind.-London.* 5, 384-386 (1999).
- [6] Lakes, R. Foam structure with a negative Poisson's ratio. *Science.* 235, 1038-1040 (1987).
- [7] Hou, X., Hu, H. & Silberschmidt, V. A novel concept to develop composite structures with isotropic negative Poisson's ratio: Effects of random inclusions. *Compos. Sci. Technol.* 72, 1848-1854 (2012).
- [8] Hou, J., Li, D. & Dong, L. Mechanical behaviors of hierarchical cellular structures with negative Poisson's ratio. *J. Mater. Sci.* 53, 10209-10216 (2018).
- [9] Grima, J.N., Mizzi, L., Azzopardi, K.M. & Gatt, R. Auxetic Perforated Mechanical Metamaterials with Randomly Oriented Cuts. *Adv. Mater.* 28, 385-389 (2016).
- [10] Prawoto, Y. Seeing auxetic materials from the mechanics point of view: A structural review on the negative Poisson's ratio. *Comp. Mater. Sci.* 58, 140-153 (2012).
- [11] Yu, L., Yan, Q. & Ruzsinszky, A. Negative Poisson's ratio in 1T-type crystalline two-dimensional transition metal dichalcogenides. *Nat. Commun.* 8 (2017) 15224.
- [12] Mistry, D., Connell, S. D., Mickthwaite, S. L., Morgan, P. B., Clamp, J. H., & Gleeson, H. F.. Coincident molecular auxeticity and negative order parameter in a liquid crystal elastomer. *Nat. Commun.* 9 (2018) 5095.
- [13] Scarpa, F. Auxetic materials for bioprostheses. *IEEE Signal. Proc. Mag.* 25, 126-128 (2008).
- [14] Ho, D.T., Park, S., Kwon, S., Park, K. & Kim, S.Y. Negative Poisson's ratios in metal nanoplates. *Nat. Commun.* 5 (2014) 3255.
- [15] Duncan, O., Allen, T., Foster, L., Senior, T. & Alderson, A. Fabrication, characterisation and modelling of uniform and gradient auxetic foam sheets. *Acta. Mater.* 126, 426-437 (2017).
- [16] Lu, Z., Li, X., Yang, Z. & Xie, F. Novel structure with negative Poisson's ratio and enhanced Young's modulus. *Compos. Struct.* 138, 243-252 (2016).
- [17] Rocklin, D.Z., Zhou, S., Sun, K. & Mao, X. Transformable topological mechanical metamaterials. *Nat. Commun.* 8 (2017) 14201.

- [18] J.N. Grima, S. Winczewski, L. Mizzi, M.C. Grech, R. Cauchi, R. Gatt, D. Attard et al. Tailoring Graphene to Achieve Negative Poisson's Ratio Properties. *Adv. Mater.* 27, 1455-1459 (2015).
- [19] J.N. Grima, M.C. Grech, J.N. Grima-Cornish, R. Gatt, D. Attard, Giant Auxetic Behaviour in Engineered Graphene, *Ann. Phys.* (2018).1700330.
- [20] Qin, H., Sun, Y., Liu, J.Z., Li, M. & Liu, Y. Negative Poisson's ratio in rippled graphene. *Nanoscale* 9, 4135-4142 (2017).
- [21] Jiang, J., Chang, T., Guo, X. & Park, H.S. Intrinsic Negative Poisson's Ratio for Single-Layer Graphene. *Nano. Lett.* 16, 5286-5290 (2016).
- [22] Ho, V.H., Ho, D.T., Kwon, S. & Kim, S.Y. Negative Poisson's ratio in periodic porous graphene structures. *Phys. Status Solid (b)* 253, 1303-1309 (2016).
- [23] Zhang, J. & Xiong, Q. The negative Poisson's ratio in graphene-based carbon foams. *Phys. Chem. Chem. Phys.* 20, 4597-4605 (2018).
- [24] Rysaeva, L.K., Lisovenko, D.S., Gorodtsov, V.A. & Baimova, J.A. Stability, elastic properties and deformation behavior of graphene-based diamond-like phases. *Comp Mater Sci* 172, 109355 (2020).
- [25] Rysaeva, L.K. et al. Elastic properties of diamond-like phases based on carbon nanotubes. *Diam Relat Mater* 97, 107411 (2019).
- [26] Zhao, Z., Wang, E. F., Yan, H., Kono, Y., Wen, B., & Bai, L., et al. Nanoarchitected materials composed of fullerene-like spheroids and disordered graphene layers with tunable mechanical properties. *Nat. Commun.* 6 (2015) 6212.
- [27] Huang, C. & Chen, L. Negative Poisson's Ratio in Modern Functional Materials. *Adv. Mater.* 28, 8079-8096 (2016).
- [28] Wen, Y., Gao, E., Hu, Z., Xu, T., Lu, H., et al. Chemically modified graphene films with tunable negative Poisson's ratios. *Nat. Commun.* 10 (2019) 2446.
- [29] Tang, D., Wang, Q., Wang, Z., Liu, Q., Zhang, B., He, D., et al. Highly sensitive wearable sensor based on a flexible multi-layer graphene film antenna. *Sci. Bull.* 63, 574-579 (2018).
- [30] Peng, L., Xu, Z., Liu, Z., Guo, Y., & Gao, C. Ultrahigh Thermal Conductive yet Superflexible Graphene Films. *Adv. Mater.* 29, 1700589 (2017).
- [31] Duan, J., Gong, S., Gao, Y., Xie, X., Jiang, L., & Cheng, Q. Bioinspired Ternary Artificial Nacre Nanocomposites Based on Reduced Graphene Oxide and Nanofibrillar Cellulose. *Acs. Appl. Mater.* 2016: acsami.6b02156.

- [32] Wan, S., Li, Y., Mu, J., Aliev, A. E., & Baughman, R. H. .Sequentially bridged graphene sheets with high strength, toughness, and electrical conductivity. *Proc. Natl Acad. Sci.*, 2018, 115(21):5359.
- [33] Wen, Y., Wu, M., Zhang, M., Li, C., & Shi, G. .Topological Design of Ultrastrong and Highly Conductive Graphene Films. *Adv. Mater.*, 2017:1702831.
- [34] Wang, Z., Mao, B., Wang, Q., Yu, J., Dai, J., & Song, R., et al. Ultrahigh Conductive Copper/Large Flake Size Graphene Heterostructure Thin-Film with Remarkable Electromagnetic Interference Shielding Effectiveness. *Small* 14, 1704332 (2018).
- [35] W Zhou, C Liu, R Song, X Zeng, BW Li, et al. Flexible radiofrequency filters based on highly conductive graphene assembly films. *Appl. Phys. Lett.* 114, 113503 (2019).
- [36] Song, R., Wang, Q., Mao, B., Wang, Z., Tang, D., & Zhang, B., et al. Flexible graphite films with high conductivity for radio-frequency antennas. *Carbon* 130, 164-169 (2018).
- [37] Sutton, M.A., Orteu, J. & Schreier, H.W. Image correlation for shape, motion and deformation measurements-basic concepts, theory and applications. (Springer).
- [38] Dong, Y.L. & Pan, B. A Review of Speckle Pattern Fabrication and Assessment for Digital Image Correlation. *Exp. Mech.* 57, 1161-1181 (2017).
- [39] Wildenschild, D. & Sheppard, A.P. X-ray imaging and analysis techniques for quantifying pore-scale structure and processes in subsurface porous medium systems. *Adv. Mater. Resour.* 51, 217-246 (2013).
- [40] Kulkarni, M., Carnahan, D., Kulkarni, K., Qian, D. & Abot, J.L. Elastic response of a carbon nanotube fiber reinforced polymeric composite: A numerical and experimental study. *Composites Part B: Engineering* 41, 414-421 (2010).
- [41] Wen, P., Takano, N. & Kurita, D. Probabilistic multiscale analysis of three-phase composite material considering uncertainties in both physical and geometrical parameters at microscale. *Acta Mech* 227, 2735-2747 (2016).
- [42] Lions, J.L.: Some methods in the mathematical analysis of systems sand their control. Science Press p1 (1981).
- [43] Pavliotis, Grigoris, and Andrew Stuart. *Multiscale methods: averaging and homogenization.* Springer Science & Business Media, 2008.
- [44] Dagdelen, J., Montoya, J., de Jong, M. & Persson, K. Computational prediction of new auxetic materials. *Nat. Commun.* 8 (2017) 323.
- [45] Guedes, J.M., Kikuchi, N.: Preprocessing and postprocessing for materials based on the homogenization method with adaptive finite element methods. *Comput. Methods Appl. Mech. Eng.* 83, 143-198 (1990).

- [46] Huang, R. et al. Porous Graphene Films with Unprecedented Elastomeric Scaffold-Like Folding Behavior for Foldable Energy Storage Devices. *Adv. Mater.* 30, 1707025 (2018).
- [47] Grima-Cornish, J.N., Grima, J.N. & Evans, K.E. On the Structural and Mechanical Properties of Poly(Phenylacetylene) Truss-Like Hexagonal Hierarchical Nanonetworks. *physica status solidi (b)* 254, 1700190 (2017).
- [48] Li, B., Cao, Y., Feng, X. & Gao, H. Mechanics of morphological instabilities and surface wrinkling in soft materials: a review. *Soft Matter* 8, 5728-5745 (2012).
- [49] Blunt, M. J., Bijeljic, B., Dong, H., Gharbi, O., Iglauer, S., & Mostaghimi, P., et al. Pore-scale imaging and modelling. *Adv. Water Resour.* 51, 197-216 (2013).

Fig.1
[Click here to download high resolution image](#)

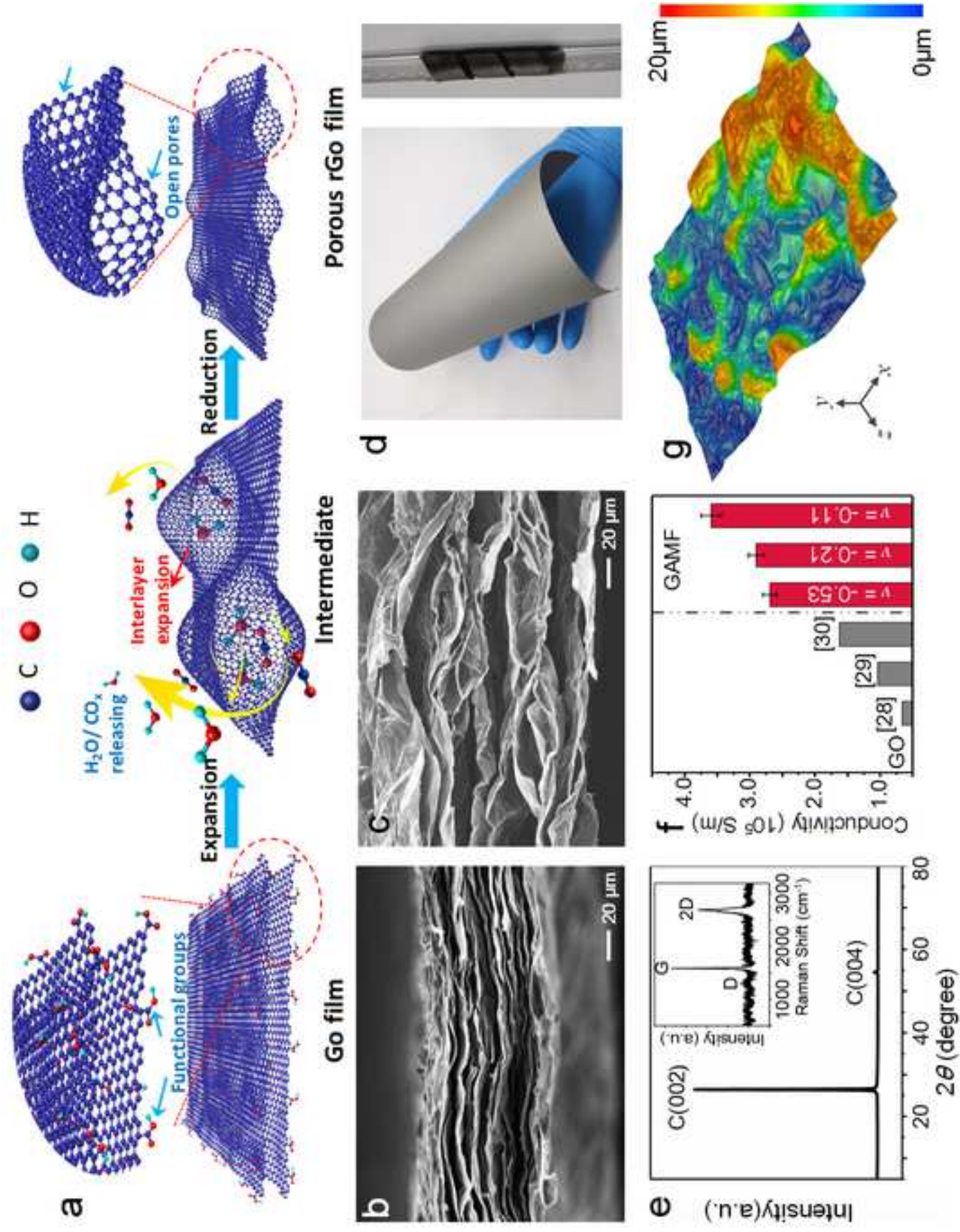


Fig.2
[Click here to download high resolution image](#)

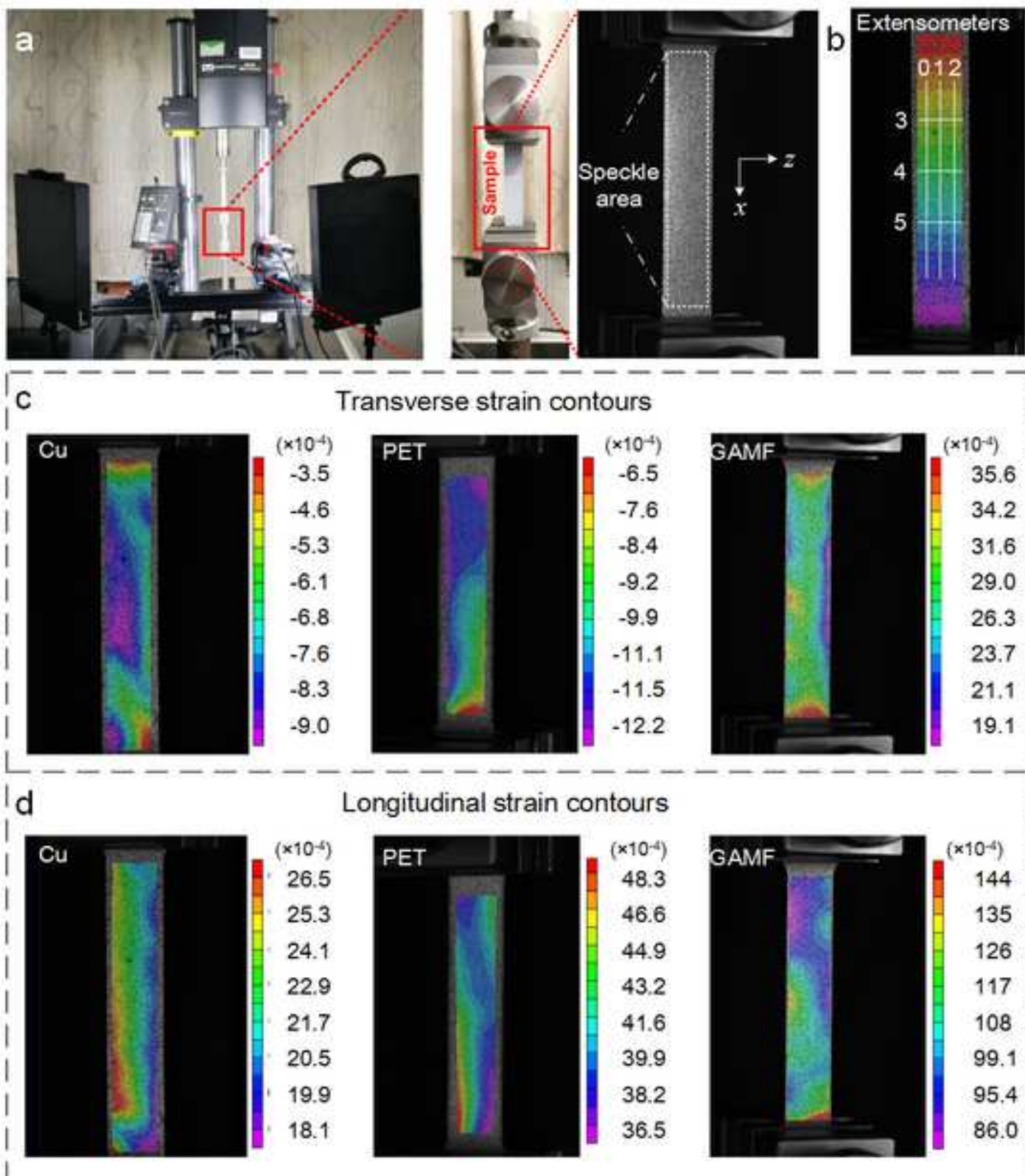


Fig.3
[Click here to download high resolution image](#)

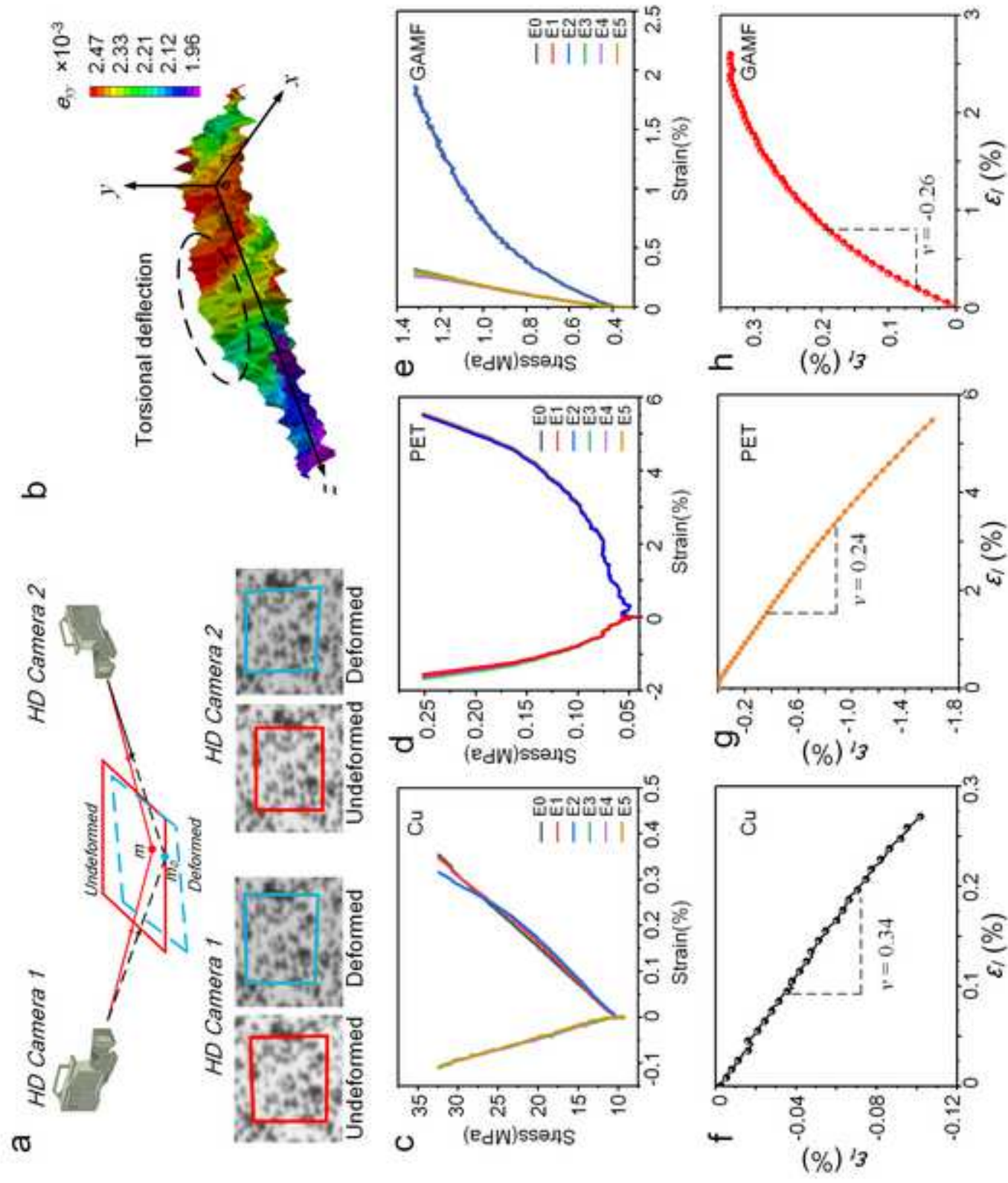


Fig.4
[Click here to download high resolution image](#)

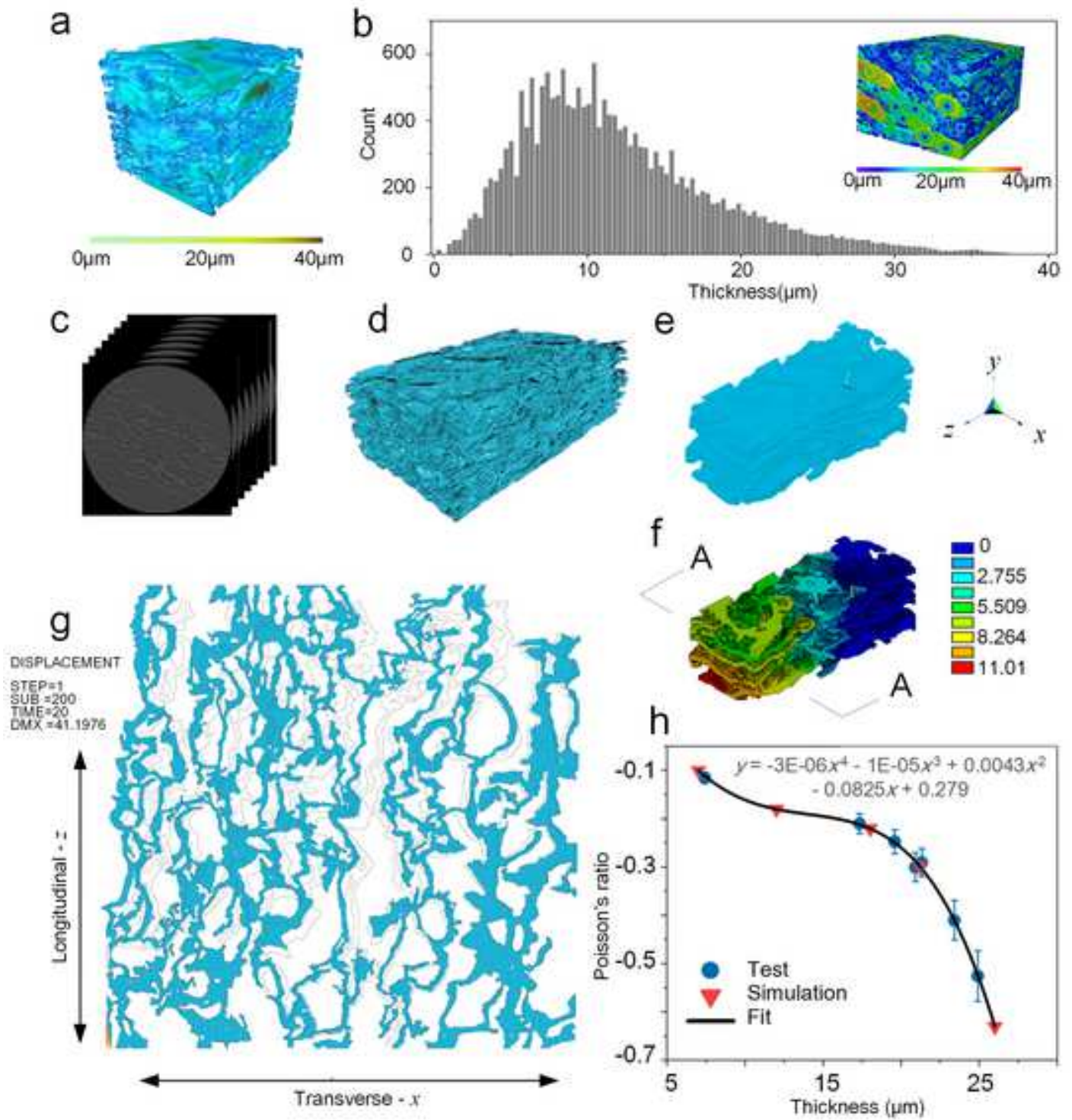


Fig.S1
[Click here to download high resolution image](#)

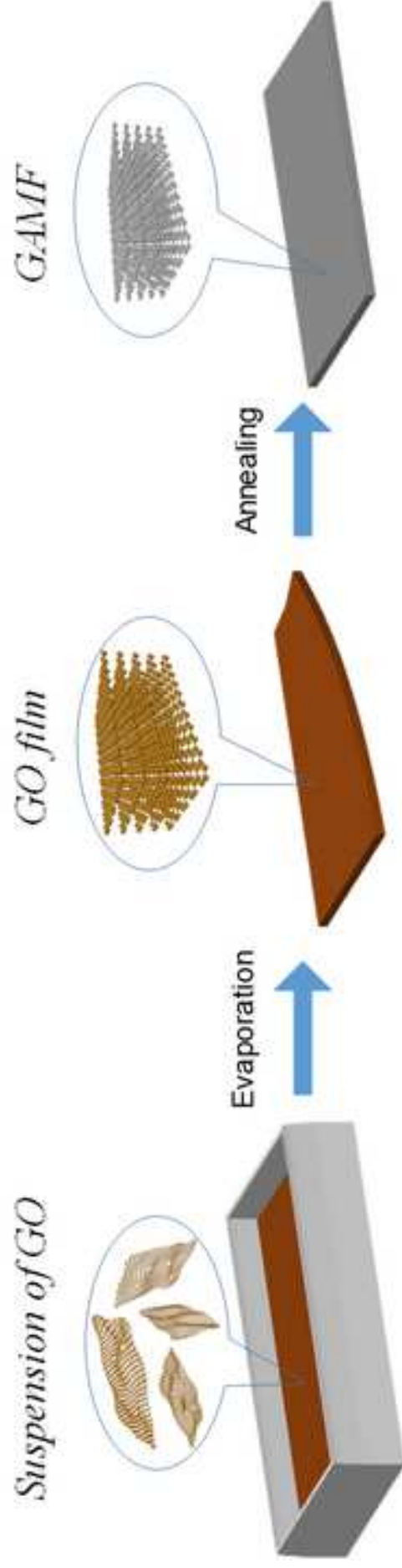
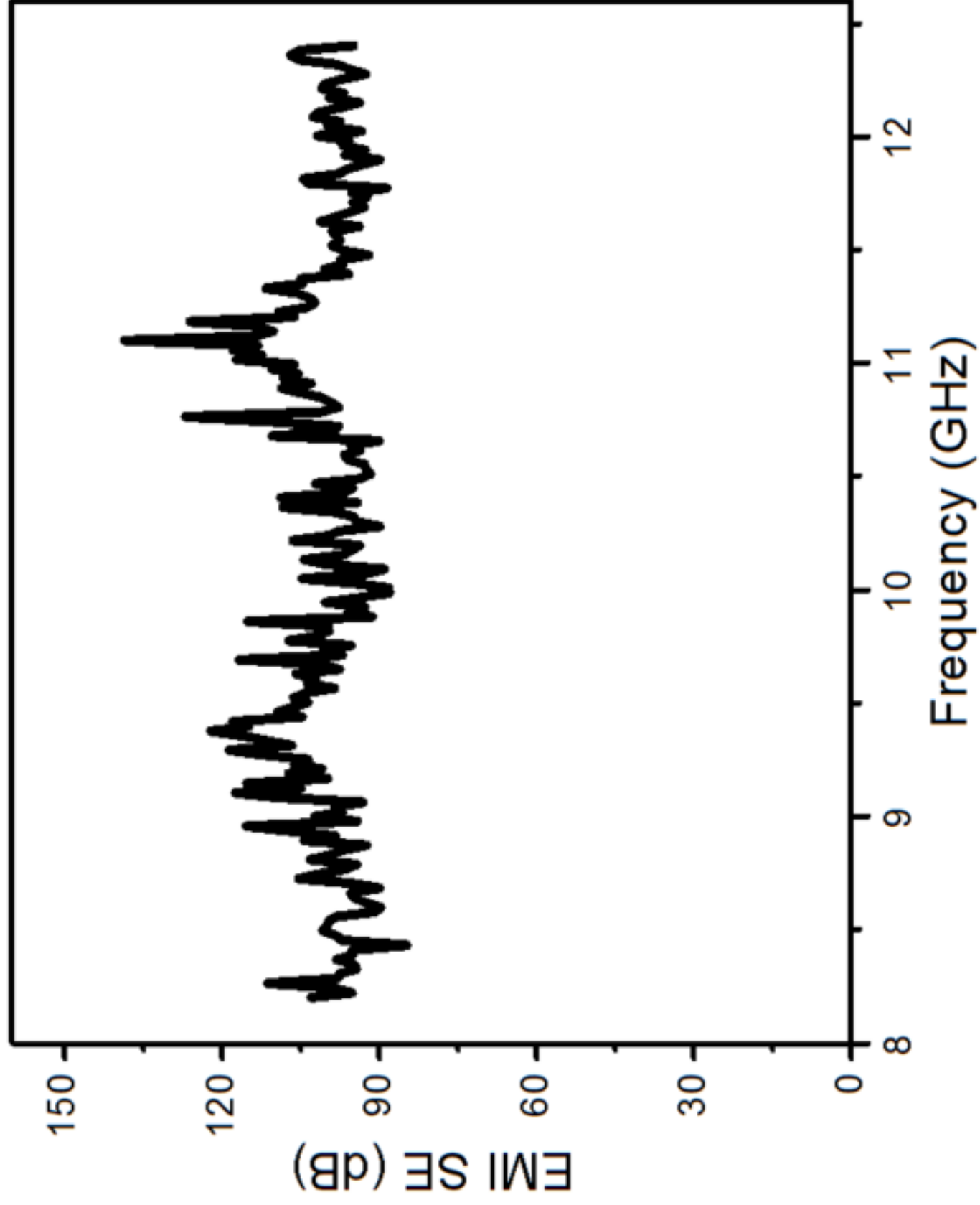


Fig.S2
[Click here to download high resolution image](#)



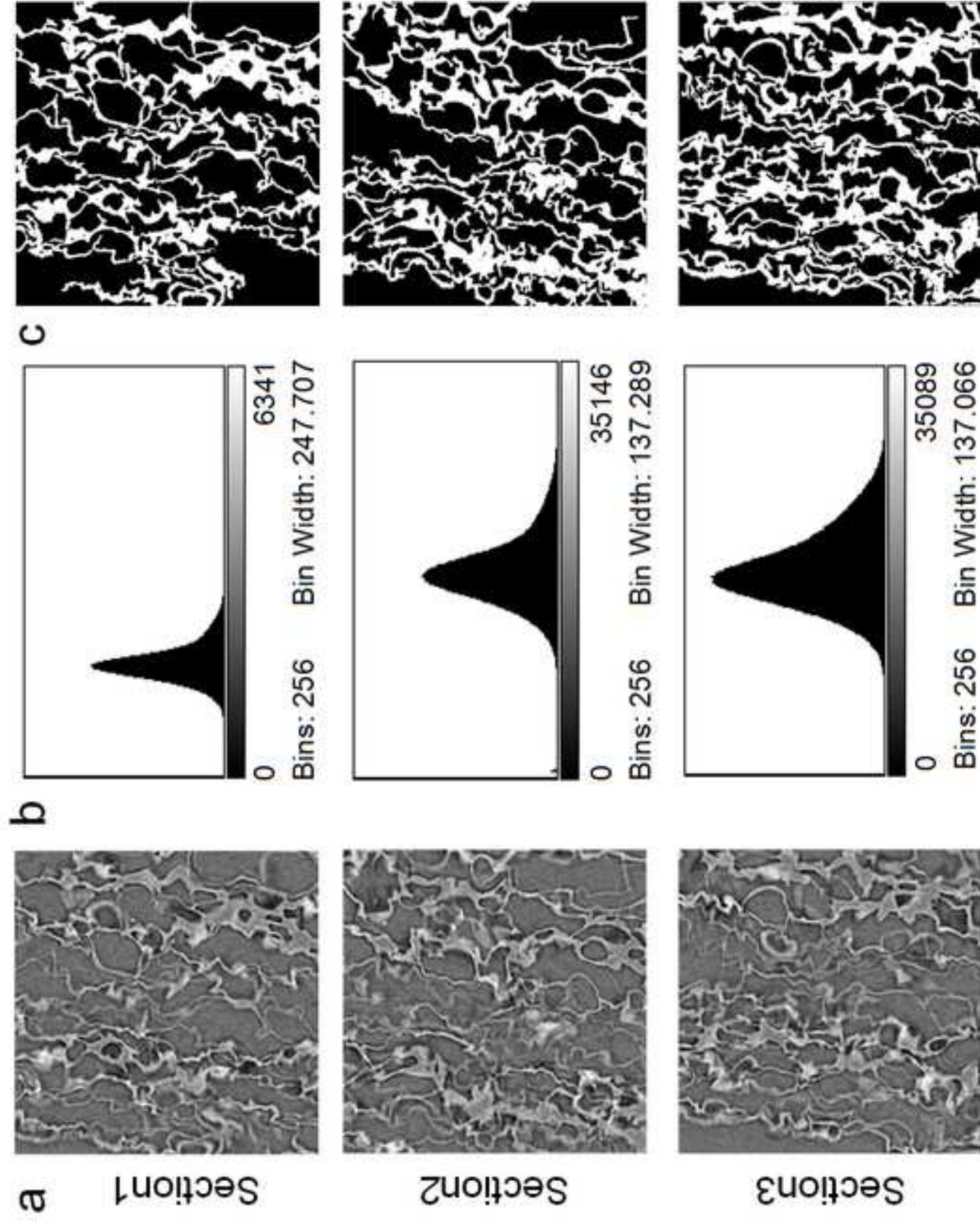


Fig.S4
[Click here to download high resolution image](#)

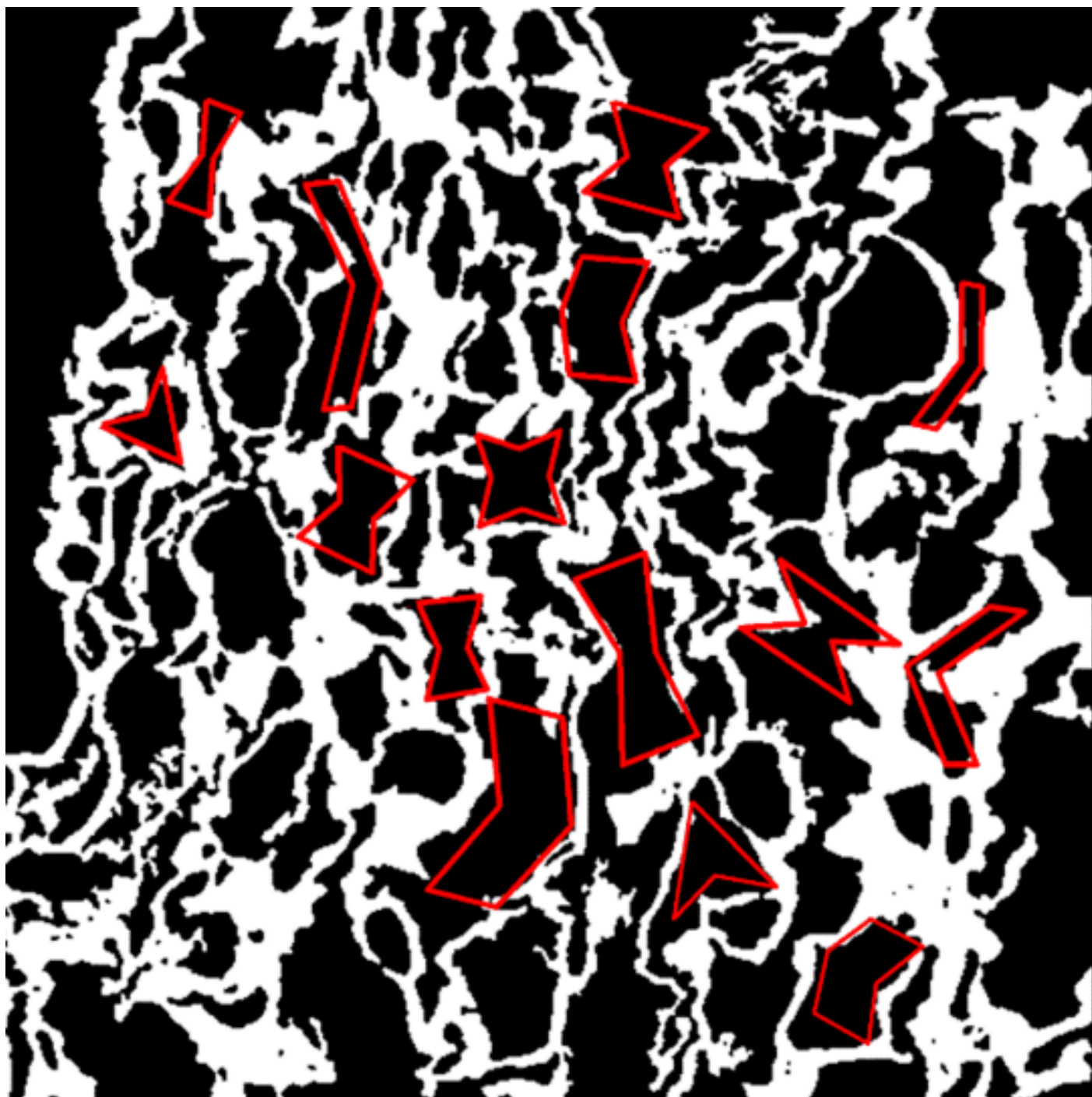
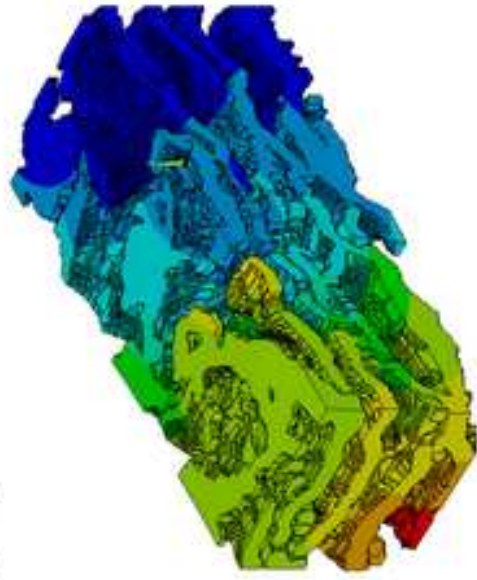
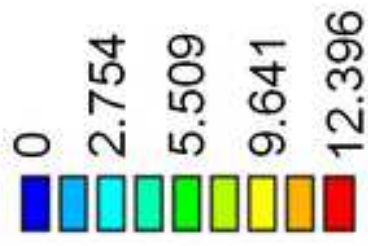
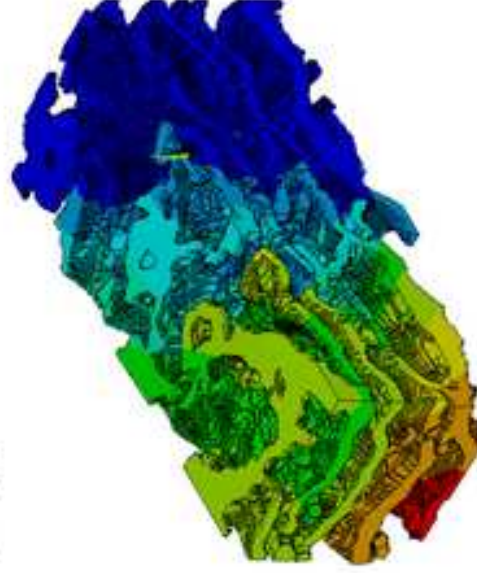


Fig.S5
[Click here to download high resolution image](#)

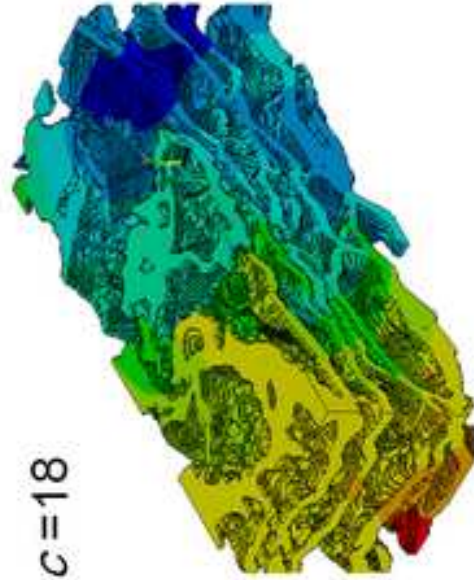
$c=7$



$c=12$



$c=18$



$c=26$

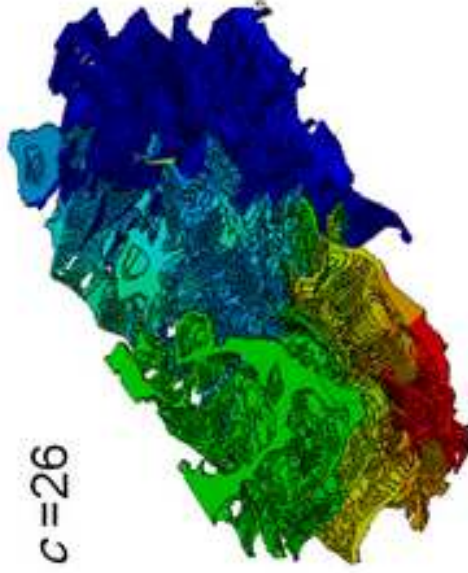


Fig.S6

[Click here to download high resolution image](#)

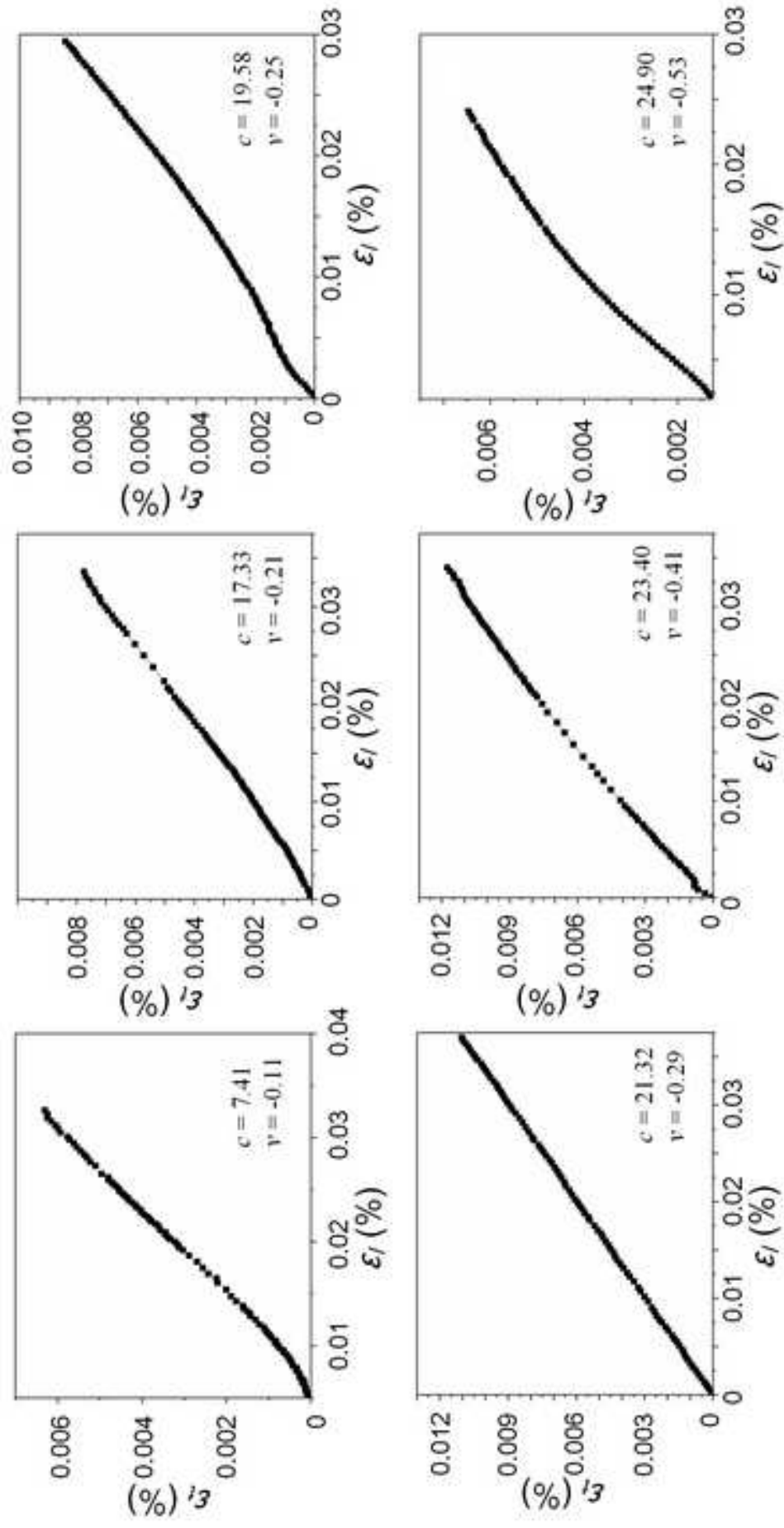
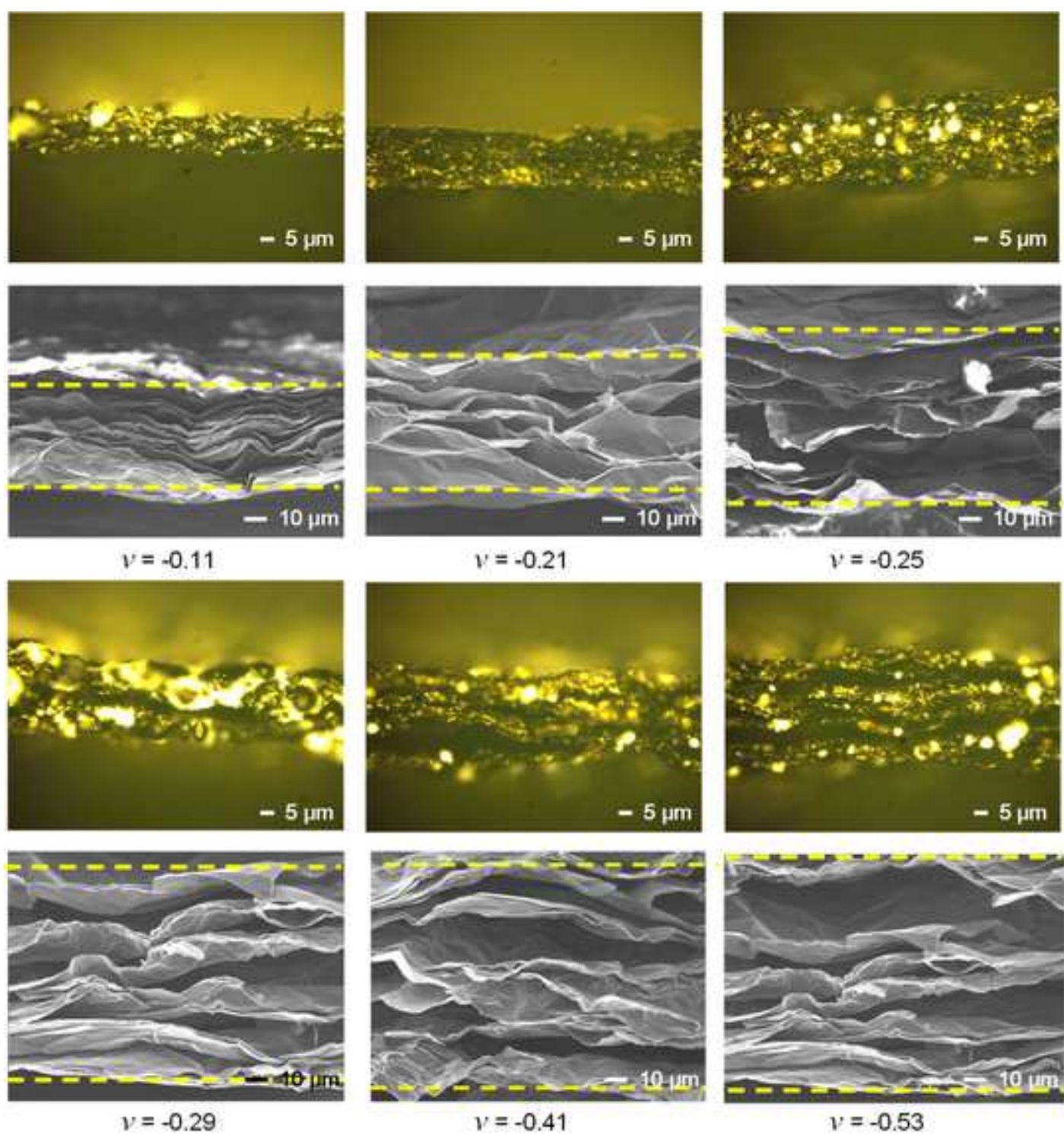


Fig.S7
[Click here to download high resolution image](#)



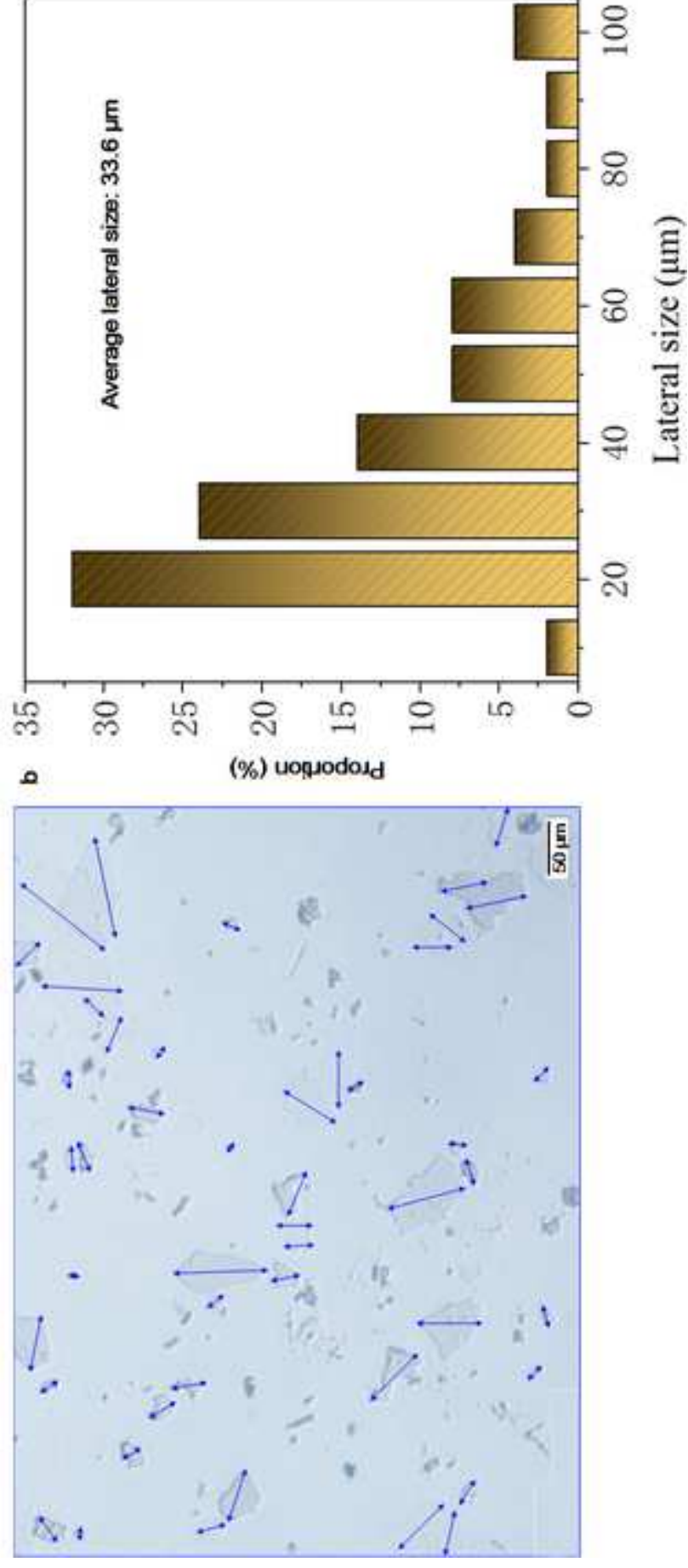
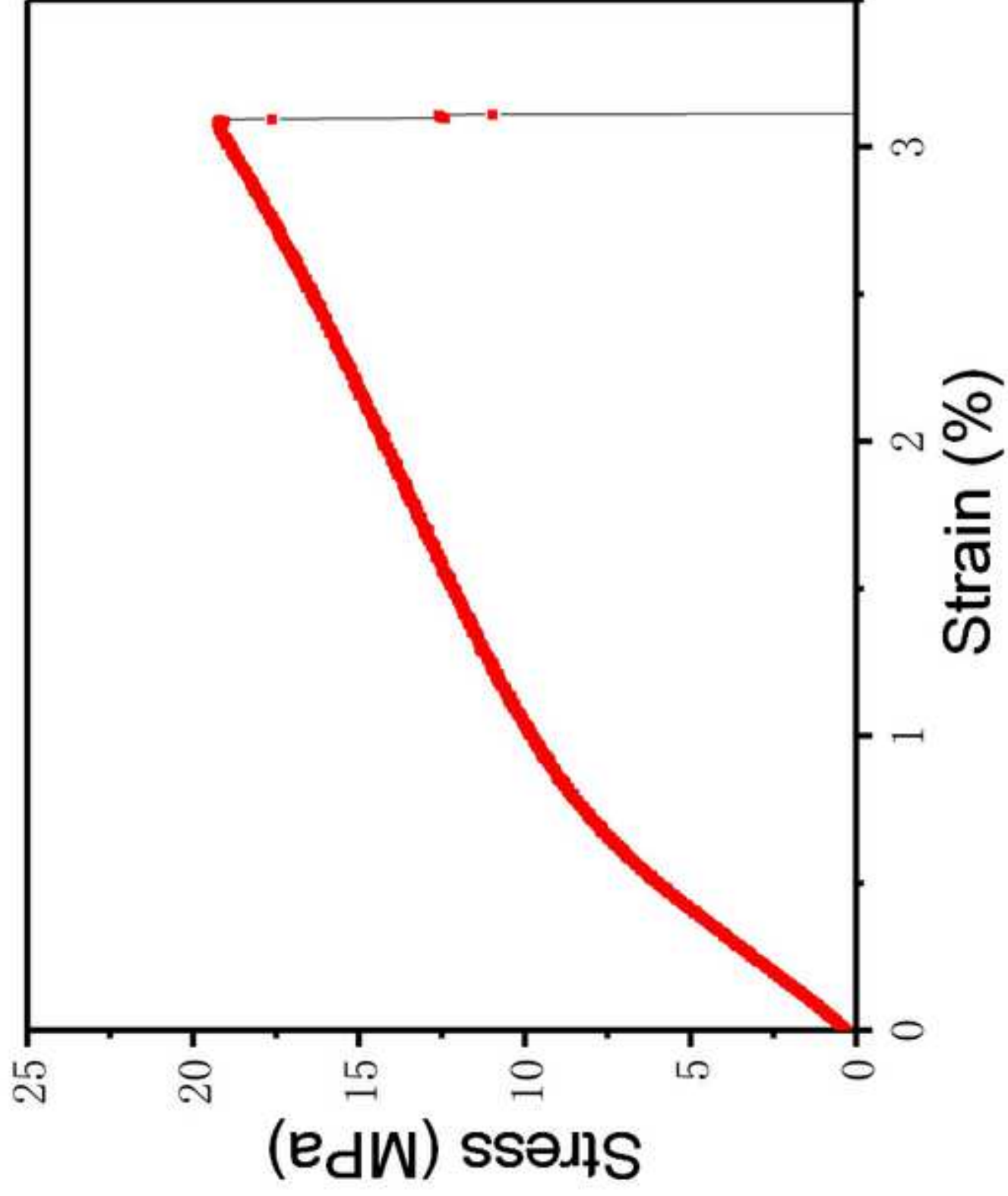
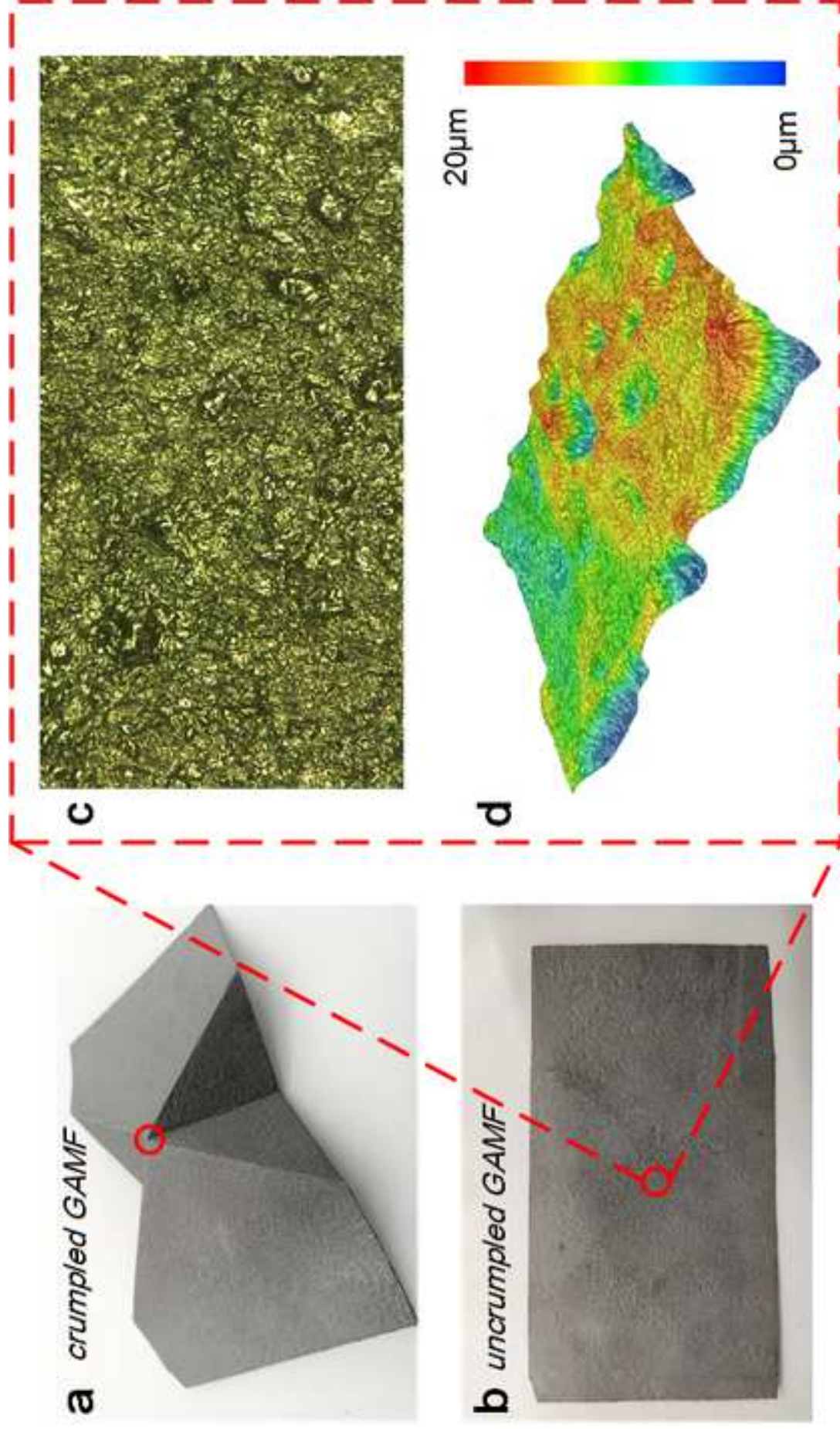
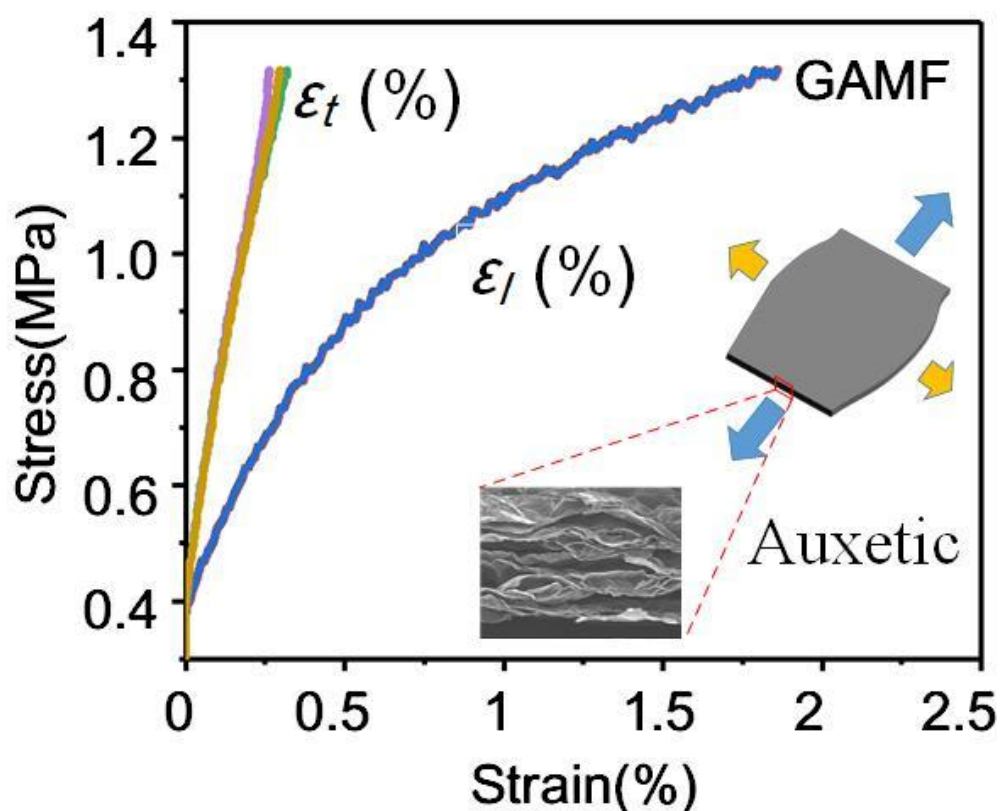


Fig.S9
[Click here to download high resolution image](#)





Customizable Fabrication for Auxetic Graphene Assembled Macrofilms with High Conductivity and Flexibility



Microporous structure was constructed as determining factor in auxetic performance of fabricated GAMF with high conductivity and outstanding flexibility through graphitization of treated graphene oxide precursor. The simulation results showed that critical thickness had an impact on NPR performance. GAMFs with different critical thicknesses were fabricated and Poisson's ratios ranging from -0.11 to -0.53 were recorded, which aligned well with the predictions and suggesting promising applications in flexible sensor devices and wearable electronic engineering.